RESEARCH ARTICLE

Check for updates

2D hetero-nanostructured reduced-CuNiFe-oxides with self-produced H$_2$O$_2$ Fenton-like photocatalysis for tetracycline degradation†

Lin Fu,‡[a] Dandan Wu, [iD] ‡[b] Ming Wen, [iD] *[a] Yuanzheng Zhu,[a,c] Qingsheng Wu [iD] [a] Tao Zhou[d] and Yongqing Fu [iD] [e]

Fenton-like photocatalysis, an advanced oxidation technology, is considered a promising method by which to degrade tetracycline antibiotic (TC) pollutants, but it remains a challenge to achieve a high degradation efficiency in an environmental friendly way. Herein, cluster structures assembled by 2D nanosheets of reduced CuNiFe mixed-metal-oxides (re-CuNiFe-MMOs) have been synthesized through a combined hydrothermal and polyols-solvothermal reduction process. The synergistic effect induced by multiphases of MMOs and the CuNi alloy endows the obtained re-CuNiFe-MMOs with superior Fenton-like photocatalytic activity for the degradation of TCs without the use of any additional oxidants, which is mainly attributed to the reactive oxygen species (of which $^{\bullet}O_2^-$ is dominant) generated under visible light based on the synergy of the multiphases. The degradation rate of TC reaches 100% in just 4 minutes with a constant reaction rate of 1.65 min^{-1}, and this can be maintained at 95.5% after 12 cycles. This study provides an environmentally friendly approach for the treatment of antibiotic pollutants directly using visible light.

1. Introduction

Tetracycline antibiotics (TCs) are widely applied to treat human and animal diseases due to their low cost and excellent antibacterial activities.[1] However, owing to their long half-life and poor biodegradation characteristics, a large amount of TC residue has accumulated in water sources, which seriously threatens ecosystems and the health of human beings and animals.[2–4] Therefore, it is crucial to explore a cheap, safe and effective way to degrade TC contaminants.

The advanced oxidation process (AOP) has been considered one of the promising ways to degrade various types of organic pollutants (*e.g.* antibiotics) into low- or non-toxic small mole-

[a]*School of Chemical Science and Engineering, The State Key Laboratory of Pollution Control and Resource Reuse, Shanghai Key Laboratory of Chemical Assessment and Sustainability, Tongji University, Shanghai 200092, P. R. China.*
E-mail: m_wen@tongji.edu.cn
[b]*School of Materials Science and Engineering, Shanghai Institute of Technology, Shanghai 201418, P. R. China*
[c]*School of Materials and Chemistry, University of Shanghai for Science and Technology, Shanghai, 200093, P. R. China*
[d]*School of Environmental Science and Engineering, The State Key Laboratory of Pollution Control and Resource Reuse, Tongji University, Shanghai 200092, P. R. China*
[e]*Faculty of Engineering and Environment, Northumbria University, Newcastle upon Tyne, NE99 1ST, UK*
†Electronic supplementary information (ESI) available. See DOI: https://doi.org/10.1039/d2qi02056d
‡These authors contributed equally to this work.

cules in water, because it can generate various types of reactive oxygen species (ROSs) to accelerate the degradation reactions.[5] Recently, the Fenton and photocatalysis methods became popular for the degradation of toxic contaminants.[6] Unfortunately, the effectiveness of the Fenton processes is strongly dependent on the pH value of the solutions. They often require a large amount of oxidizing agent such as hydrogen peroxide (H$_2$O$_2$) or persulfate, and also produce large amounts of iron sludge, which are difficult to separate from the catalyst afterwards.[7] Additionally, although the photocatalysis can use ROSs produced by photogenerated electrons (e$^-$) and holes (h$^+$) to oxidize and degrade antibiotics,[8] it is limited by poor visible light utilization and lots of recombination of e$^-$ and h$^+$.[9] Photocatalysts with multiphases of metal and semiconductor are expected to solve the above-mentioned problems. They can be readily modified to adjust their bandgaps, efficiently transfer interfacial charges, and significantly reduce recombination of photogenerated e$^-$ and h$^+$. Therefore, their use has now become one of the effective ways to improve the degradation efficiency.[10] Transition metals (such as Cu, Fe, and Co) can produce different valence states to form multiphase interfaces (*e.g.* biochar modified CuFeO$_2$, CuFe$_2$O$_4$/Bi$_2$O$_3$, and CuCo$_2$S$_4$).[11–13] In addition, the efficient transfer of e$^-$ or h$^+$ greatly promotes the production of active free radicals, enhancing the catalytic degradation performance.[14,15] If the electrons and abundant H$_2$O$_2$ produced by the photocatalysis can be directly used in the Fenton-like process, it will avoid the use of oxidants and simultaneously promote the effective

This journal is © the Partner Organisations 2023

Inorg. Chem. Front., 2023, **10**, 567–578 | **567**

separation of photogenerated e^-/h^+ pairs. Hence, synergy of the photocatalysis and Fenton-like effects can be applied to generate highly reactive free radicals without an oxidant, thus improving the efficiency of oxidative degradation.

The microstructure of the catalyst is an important factor influencing its photocatalytic performance.[16] Two-dimensional (2D) ultrathin heterostructures have large photosensitive surfaces, which can shorten the carriers' migration distance, provide multiple surface reaction sites, and reduce the energy barrier for reactions, all of which are favorable for the effective migration and transfer of photogenerated carriers to achieve superior catalytic performance.[17–19] It is worth mentioning that the nanosheet-assembled clusters not only have the features of 2D ultrathin heterostructures, but also provide stable structures to prevent severe agglomeration of the nanosheets.[20–23] Therefore, these 2D ultrathin heterostructure-based Fenton-like photocatalysts containing multiphases of metals and semiconductors are effective in solving the problem of antibiotic contamination in an environmentally friendly manner.

In this study, a cluster structure assembled by 2D nanosheets of reduced CuNiFe mixed-metal-oxides (re-CuNiFe-MMOs) (Fig. 1) has been successfully synthesized through a combined hydrothermal and polyol solvothermal reduction (HPSR) process. When used as a Fenton-like photocatalyst but without adding H_2O_2, these re-CuNiFe-MMOs nanosheets can achieve an outstanding degradation efficiency for TCs, including tetracycline (TC), chlortetracycline (CTC) and oxytetracycline (OTC). The excellent performance has been assigned to the following reasons. (1)

The cluster structure assembled by the re-CuNiFe-MMOs nanosheets can offer a large specific surface area and expose more active sites, which are beneficial to the catalytic degradation process; (2) the re-CuNiFe-MMOs with multiple nanophases (including CuNi, Cu_2O, CuO, FeO and NiO) have adjustable bandgaps and can facilitate effective electron transfer, both of which improve the utilization of visible light; (3) the synergy of photocatalysis and the Fenton-like effect not only results in a high oxidative degradation ability for TCs, but also avoids the use of strong oxidants in the Fenton-like process, which can be produced by the photocatalysis process and hydroxyl oxidation on the surface of the catalyst; (4) a large number of defects (*e.g.* oxygen vacancies (OVs)) formed by the *in situ* reduction of CuNiFe-MMOs can react with oxygen molecules and provide more ROSs, thus accelerating the degradation rate of the TCs. Based on the above analysis, the synergetic effects of the CuNi-nanophase, FeO and Cu mixture oxides can effectively enhance Fenton-like photocatalysis towards the degradation of TCs without the need for oxidants. Therefore, this study is of great significance in the development of an environment friendly approach for the highly efficient treatment of TC pollution without oxidants.

2. Experimental

2.1. Synthesis of re-CuNiFe-MMOs

The chemical reagents used in the experiments are described in the ESI Text S1.† The heterostructure clusters assembled by
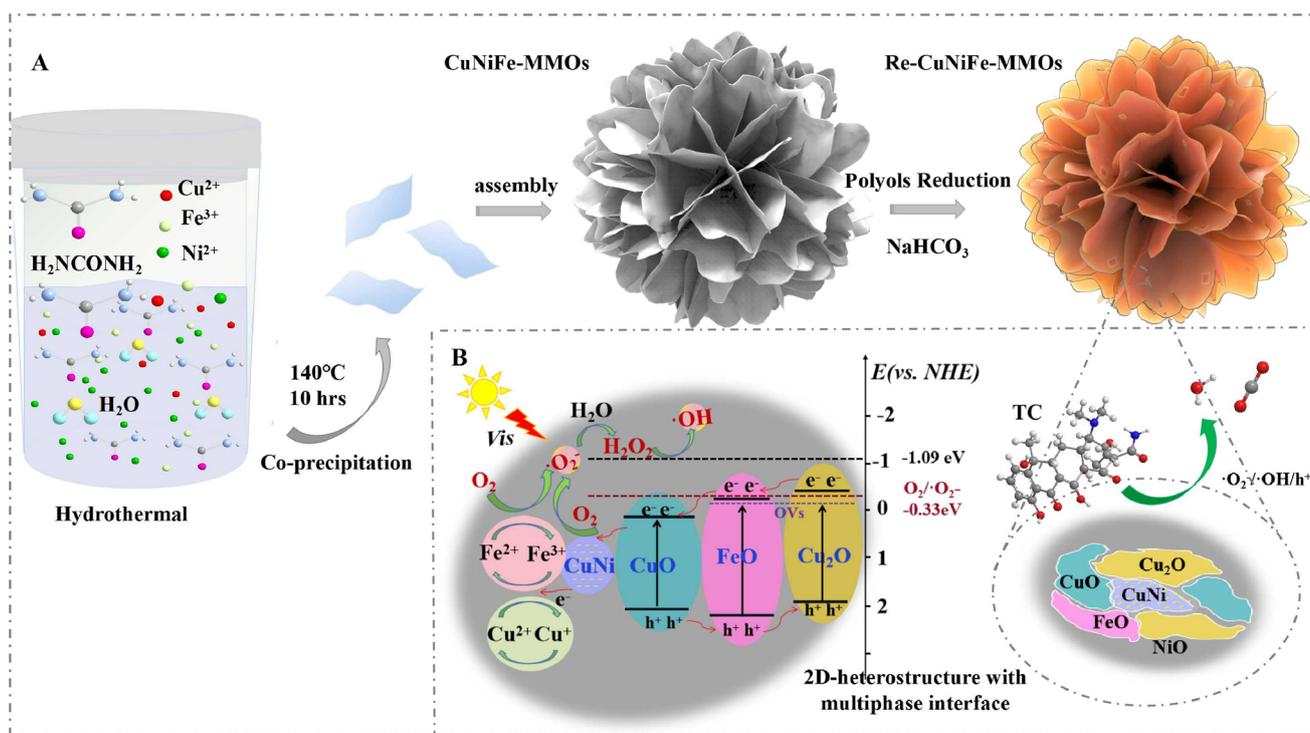

Fig. 1 Schematic illustration of (A) the fabrication of the re-CuNiFe-MMOs 2D-heterostructure and (B) its Fenton-like photocatalytic mechanism for TC degradation.

the re-CuNiFe-MMOs nanosheets were fabricated through the HPSR method based on the following procedures. $Cu(NO_3)_2\cdot3H_2O$ (4 mL, 10 mM), $Fe(NO_3)_3\cdot9H_2O$ (4 mL, 10 mM), and $Ni(NO_3)_2\cdot6H_2O$ (5 mL, 20 mM) were mixed first, then urea (6 mL, 10 mM) was added into the mixture with continuous stirring for 30 min. After the mixture had been heat-treated at 140 °C for 10 h inside a 25 mL Teflon-lined stainless-steel autoclave, the CuNiFe-MMOs precursor was obtained. This precursor and 10 mg of $NaHCO_3$ were then mixed with 15 mL of ethylene glycol, followed by a solvothermal reduction process performed at 160 °C for 2 h. After the reaction solution had been naturally cooled down to room temperature, the re-CuNiFe-MMOs were collected by washing alternately with water and ethanol three times and then dried under vacuum at 60 °C for 2 h. The preparation methods of the re-CuFe-MMOs, re-CuNi-MMOs, and re-FeNi-MMOs were similar to those of the re-CuNiFe-MMOs, except that Ni, Fe and Cu, respectively, were not available in the raw materials.

2.2. Characterization methods

The microstructures and morphology of the samples were characterized using a field emission scanning electron microscope (FE-SEM, JEOL, S-4800), and a transmission electron microscope (TEM, JEOL JEM-2100) with a selective region electron diffraction (SAED) function. The element distribution inside the samples was detected using an energy-dispersive X-ray spectrometer (EDS, TN5400, 15 keV). The crystalline structures of the samples were measured using powder X-ray diffraction (XRD, Bruker D8, with Cu Kα as the source of radiation). The surface area of the prepared materials was measured using a Brunauer–Emmett–Teller (BET, Micromeritics TRISTAR 3020 V) method. Surface functional groups were analyzed using a Fourier transform infrared spectroscope (FT-IR, Nicolet IS10). Molecular structures were studied using a Raman spectroscope (InVia microconfocal spectrometer, Renishaw Corporation) with a He–Ne laser at a wavelength λ of 514 nm and a power of 10–20 mW. The element bonding and valence band positions (E_{VB}) were studied using an X-ray photoelectron spectroscope (XPS, PHI-5000C ESCA system) with Al Kα as the radiation source, and calibrated using C 1s of the surface contaminant at 284.6 eV. UV-vis diffuse reflectance spectroscopy (Cary 5000 UV-Vis-NIR with a Pb smart detector) was used to monitor the bandgaps of the materials under the wavelength range of 200–800 nm. The efficiency of the photogenerated charge transfer was tested using a photoluminescence spectroscope (PL, F-7000, Hitachi Limited). Analysis using electrochemical impedance spectroscopy (EIS) was performed using an electrochemical workstation (CHI660E, Shanghai Chenhua). Electron paramagnetic resonance (EPR) spectra (Miniscope MS-5000 EPR spectrometer at 293 K) were recorded with 5,5-dimethyl-1-pyrroline N-oxide (DMPO) and 2,2,6,6-tetramethylpiperidine (TEMP) used as spin probes.

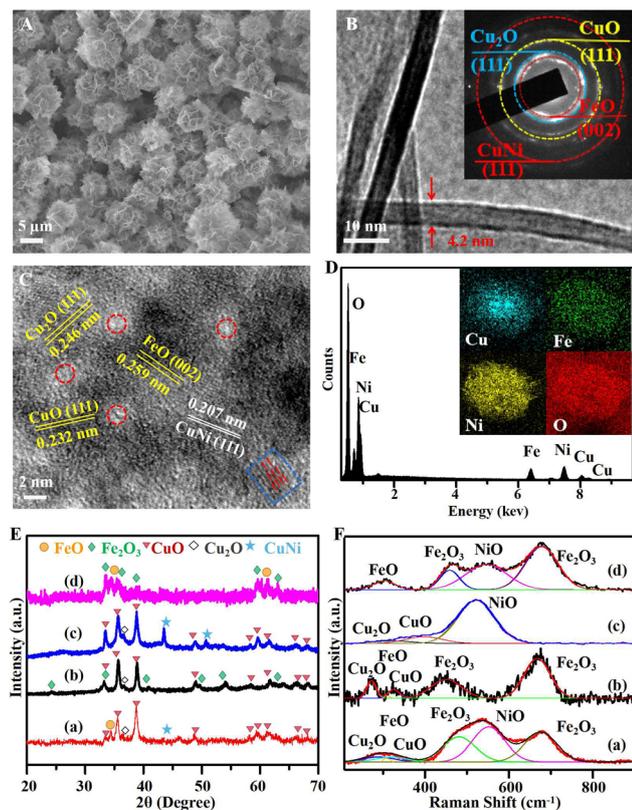### 2.3. Assessment of Fenton-like photocatalytic performance

The Fenton-like photocatalytic activity of the prepared catalysts against TCs (including tetracycline, chlortetracycline, and oxy-

tetracycline), and non-tetracycline antibiotics ampicillin (AMP) and kalamycin (KAN) were tested using multi-tube photocatalytic reaction equipment (JOYN-GHX-BC, Shanghai Joyn Electronic CO., Ltd) with a 150 W Xe lamp, which was equipped with a cut-off filter ($\lambda > 420$ nm) to obtain a visible light source. In the experiments, 10 mg of the catalyst was first mixed into an antibiotic solution (40 mL, 10 mg L^{-1}), and kept in the dark under N_2 for 30 min to achieve an adsorption–desorption equilibrium before visible-light irradiation. During the degradation of the TCs, 3 mL of the suspension was removed regularly with a 0.22 µm wavelength filter. The concentration of TC was determined based on its absorbance wavelength using a UV-vis spectrophotometer (UV-1800, Shimadzu). The intermediates generated during the degradation process were analyzed using liquid chromatography-mass spectrometry (LC-MS, Varian 310). The mineralization efficiency was quantified using a total organic carbon (TOC) analyzer (TOC-VCPH, Shimadzu). For identifying the contribution of ROSs, radical trapping tests were performed by adding scavengers into a mixed solution of antibiotics, including triethanolamine (TEA, 1 mM), benzoquinone (BQ, 0.01 mM), isopropanol (IPA, 1 mM), and furfuryl alcohol (FFA, 1 mM). To detect superoxide radicals ($^{\bullet}O_2^{-}$) and hydroxyl radicals ($^{\bullet}OH$), 10 mg of sample powder and 10 µL of DMPO were evenly dispersed in 2 mL of deionized water, then the suspensions were illuminated under a 150 W Xe lamp with a UV cutoff filter ($\lambda > 420$ nm) for 4 min and the supernatants of the suspension were collected for analysis using EPR spectroscopy. Meanwhile, using the same detection method as described above, TEMP was used as a spin trap to detect singlet oxygen ($^1O_2$). For evaluating the degradation of TC into CO_2, H_2O, and other inorganic small molecules, 50 mg L^{-1} of TC was subjected to Fenton-like photocatalytic degradation, and 20 mL of the suspension was taken out regularly with a 0.22 µm filter. Finally, E. coli culture experiments were performed using the solution removed above for verification (Text S2†).

3. Results and discussion

3.1. Synthesis and characterization

The Fenton-like photocatalyst of the cluster structure assembled by the re-CuNiFe-MMOs hetero-nanosheets was synthesized through the HPSR process, as illustrated in Fig. 1A. First, the urea is gradually hydrolyzed into ammonia and carbonate at 140 °C, which creates an alkaline condition, and thus offers plenty of nucleation sites, and CuNiFe-MMOs nanosheets are formed within the confined growth space. Then, the three-dimensional (3D) assembly of the nanosheets gradually results in the oriented arrangement of the nanosheets, which are perpendicular to each other to reduce their interaction energy (Fig. S1†).[22] Subsequently, the reduction of the CuNiFe-MMOs at 160 °C in ethylene glycol in the solvothermal system with the assistance of $NaHCO_3$ produces multimetal and multivalent re-CuNiFe-MMOs with multiphase interfaces. Fig. 2A and B show that the re-CuNiFe-

This journal is © the Partner Organisations 2023

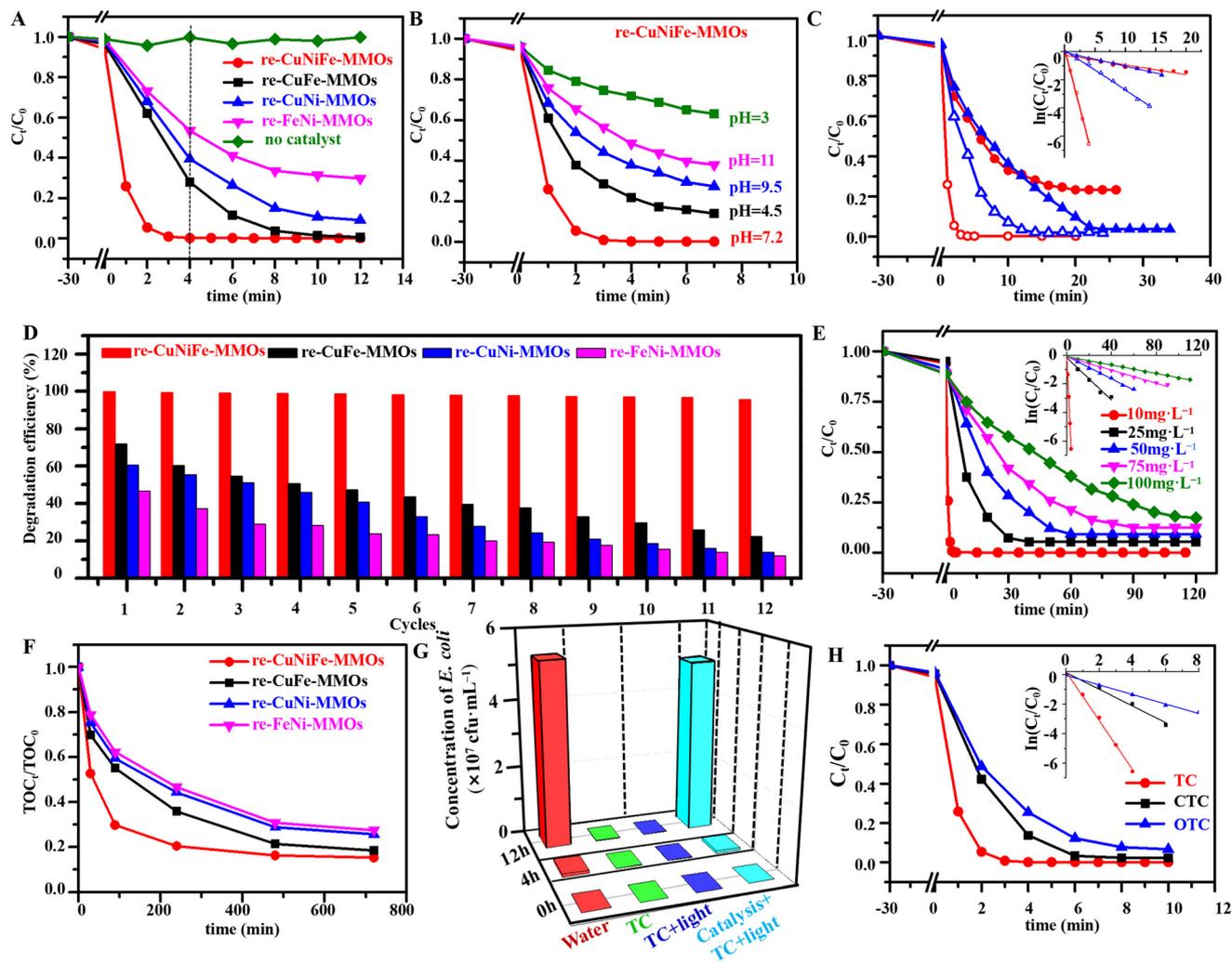*Inorg. Chem. Front.*, 2023, **10**, 567–578 | **569**

Fig. 2 (A) SEM image, (B) TEM image with the SAED pattern in the inset, (C) HRTEM image, (D) EDS pattern with elemental mapping in the inset, of the re-CuNiFe-MMOs catalyst. (E) XRD patterns and (F) Raman spectra for the re-CuNiFe-MMOs (a), re-CuFe-MMOs (b), re-CuNi-MMOs (c), and re-FeNi-MMOs (d).

MMOs have nanosheet-assembled clusters with an average nanosheet (7 layers) thickness of 4.2 nm and an average specific surface area of 126 m^2 g^{-1} (Fig. S2 and Table S1†). Such a stable cluster structure can offer a good number of exposed active sites and maximize their catalytic activities. Its SAED pattern exhibits a polycrystalline nature (Fig. 2B inset), in which different diffraction rings are identified as facets of FeO (002), Cu$_2$O (111), CuO (111), and CuNi (111). The HRTEM measurement image shows their corresponding lattice spacings of 0.259, 0.246, 0.232, and 0.208 nm (Fig. 2C). The disordered regions (marked in red circles) and the dislocations of the lattice fringes (marked in a blue circle) on the surfaces of the re-CuNiFe-MMOs nanosheets correspond to the amorphous structures or structural defects (e.g. OVs and grain boundaries).[24] Additionally, the EDS results prove the existence of Cu, Fe, Ni and O, which are uniformly distributed on the re-CuNiFe-MMOs nanosheets (Fig. 2D). In Fig. 2E, the XRD peaks of re-CuNiFe-MMOs at 35.5°, 38.7°, 48.7°, 61.5°, 66.2°, and 68.1° are attributed to the (11$\bar{1}$), (111), (20$\bar{2}$), (11$\bar{3}$), (31$\bar{1}$), and (220) faces, respectively, of CuO (JCPDS No. 48-1548). The peak of the CuNi alloy (JCPDS No. 09-0205) at 43.5° is located between those of Cu (JCPDS No. 04-0836) and Ni (JCPDS No. 65-0380). Cu$_2$O at 36.5° (JCPDS No. 65-3288) and FeO at 34.5°

(JCPDS No. 49-1447) also co-exist, while NiO remains amorphous without showing any diffraction peaks. XRD peaks of Cu oxides, Fe oxides and CuNi-alloy were not detected in the samples of re-FeNi-MMOs, re-CuNi-MMOs, and re-CuFe-MMOs, respectively. The existence of multiphases can also be confirmed by the Raman spectra (Fig. 2F). The peaks at 303, 320 and 553 cm^{-1} are assigned to the Fe–O, Cu–O, and Ni–O stretching vibration modes of FeO, CuO, and NiO, respectively.[25–27] The peak at 286 cm^{-1} is the symmetrical stretch of Cu–O in Cu$_2$O. The peaks at 480 and 675 cm^{-1} are due to the Fe–O vibration of the inevitable Fe$_2$O$_3$ in air.[28] All the above peaks can be observed in the re-CuNiFe-MMOs, whereas the peaks of Ni–O, Fe–O, and Cu–O are absent in the re-CuFe-MMOs, re-CuNi-MMOs, and re-FeNi-MMOs, respectively. For all the samples, the positions of the Fe–O and Ni–O peaks remain nearly unchanged, whereas for the re-CuNiFe-MMOs, the Cu–O peaks are red-shifted compared with those of the re-CuFe-MMOs, but are blue-shifted compared to those of the re-CuNi-MMOs.[29]

3.2. Fenten-like photocatalytic performance

The catalytic performance of the re-CuNiFe-MMOs was evaluated by UV-vis spectra for TC degradation under visible light irradiation. The ring-opening degradation of the TC molecules can be identified by two characteristic absorption peaks at 370 nm (benzene) and 245 nm (naphthalene) (Fig. S3†).[30] In this Fenton-like photocatalysis reaction system, the synergistic effect of FeO and the multivalent oxidation states of Cu significantly enhances the capability for TC degradation even without adding H$_2$O$_2$. Fig. 3A shows that with an initial TC concentration of 10 mg L^{-1} at a pH value of 7.2 and a catalyst dosage of 0.25 g L^{-1}, when no catalyst is used under visible light irradiation, very little TC is degraded. Whereas upon using the optimized re-CuNiFe-MMOs without H$_2$O$_2$ (Fig. S4–S6†), an optimal TC removal rate of 99.9% can be achieved in 4 min with a constant reaction rate (K) of 1.65 min^{-1}, which is much higher than 72.1% (K = 0.44 min^{-1}) for re-CuFe-MMOs (Fig. S7A and S8A†), 60.6% (K = 0.23 min^{-1}) for re-CuNi-MMOs (Fig. S7B and S8B†) and 46.5% (K = 0.12 min^{-1}) for re-FeNi-MMOs (Fig. S7C and S8C†). The good linear relationship between ln (C_t/C_0) and the irradiation time reveals pseudo-first-order kinetics (Fig. S8D†). Additionally, the re-CuNiFe-MMOs show a much better catalytic performance than the CuNiFe-MMOs (Fig. S9†), confirming that the Fenton-like photocatalytic activity is mainly derived from FeO and the multivalent oxidation states of Cu. Owing to the existence of amphoteric molecules, pH variation will result in different molecular forms of TC. TC exists as protonated TC$^+$ when pH < 4, whereas it is mainly in the form of neutral TC at a pH of 4–7.5. It becomes the anion TC$^-$ when pH > 7.5. Clearly, the pH value influences the adsorption capacity and performance of the catalyst. In our case, under visible light irradiation for 4 min using the re-CuNiFe-MMOs catalyst, the TC removal rate increases from 28.1% to 78.2% when the pH value is increased from 3.0 to 4.5. It can reach nearly 100% at a pH of 7.2, whereas it gradually decreases from 62.2% to 51.6% when the

570 | *Inorg. Chem. Front.*, 2023, **10**, 567–578

This journal is © the Partner Organisations 2023

Fig. 3 Profiles of (A) TC degradation catalyzed by the prepared catalysts and (B) different pH over the re-CuNiFe-MMOs. (C) Profiles of TC degradation with the inset showing the corresponding pseudo-first-order kinetic models over polyol reduced CuNiFe-MMOs (red) and H_2 reduced CuNiFe-MMOs (blue) with catalase (solid) and without catalase (hollow). (D) Graph showing the corresponding degradation efficiency in the cycling test catalyzed by the prepared catalysts. (E) Degradation for high concentrations of TC using the re-CuNiFe-MMOs catalyst. (F) TOC removal efficiency using the prepared catalysts. (G) Graph showing the reproduction concentration of *E. coli* in the solution culture after TC degradation at different times. (H) Degradation rate of TCs catalyzed by the re-CuNiFe-MMOs. (Operating parameters: after 30 min of adsorption equilibrium under anaerobic dark conditions, 0.25 g L^{-1} catalyst, 10 mg L^{-1} TC (A–D and H), 50 mg L^{-1} TC (F and G), 25 °C, pH 7.2).

pH value is further increased from 9.5 to 11.0 (Fig. 3B and Fig. S10†). This can be explained by the fact that the electron density of TC in its neutral state is much higher than those in the acidic or alkaline states, which is conducive to the attack of free radical species.[31] $^\bullet O_2^-$ is the dominant free radical at neutral pH, which maintains a high degradation efficiency of TC.[32] Whereas under acidic or basic conditions, a large amount of H^+ or OH^- will react with $^\bullet O_2^-$ or the catalyst to a certain extent, which directly affects the degradation performance of the catalyst on the TC.[33] As discussed above, polyol reduction results in multiphases and a large number of associated OVs on the catalyst surface, thus suppressing the recombination of photogenerated electrons and holes, which together with the assistance of the Fenton-like effect improves the

visible light-induced Fenton-like photocatalytic degradation performance.

In contrast, in Fig. 3C, H_2-reduced CuNiFe-MMOs (Fig. S11†) is largely inferior in performance under the same conditions as for polyol-reduced re-CuNiFe-MMOs. This is mainly due to the surface the −OH groups can produce a large amount of H_2O_2 which is involved in the Fenton-like reaction system of the re-CuNiFe-MMOs. This can be proven by catalase tests in the TC degradation process. Catalase can consume the produced H_2O_2 during the reaction with 76.8% degradation by using the polyol-reduced re-CuNiFe-MMOs catalyst, but the degradation rate hardly changed when using the H_2-reduced re-CuNiFe-MMOs catalyst. This also proves that the H_2O_2 produced by the surface -OH groups in the catalytic reaction

system of the re-CuNiFe-MMOs avoids the utilization of the additional oxidants in our Fenton-like reaction. Further investigations of recyclability and stability were performed for the re-CuNiFe-MMOs catalyst toward TC degradation. The Fenton-like photocatalytic degradation efficiency can be maintained at 95.5% over 12 cycles without showing apparent morphology changes (Fig. S12–S14 and Table S2†). The slightly decrease in the degradation performance is mainly due to the attachment of degraded intermediates on the catalyst surface. In contrast, the degradation rates of the re-CuFe-MMOs, re-CuNi-MMOs, and re-FeNi-MMOs are significantly reduced to 22.2%, 13.4%, and 11.6%, respectively, after 12 cycles, which are all much lower than that of the re-CuNiFe-MMOs (Fig. 3D). To demonstrate the applications, the re-CuNiFe-MMOs was used to catalyze the degradation of a high concentration of TC. At TC concentrations of 10, 25, 50, 75, and 100 mg L^{-1}, the obtained degradation rates were 99.9%, 94.6%, 90.8%, 87.4%, and 82.7% with K values of 1.65, 0.075, 0.040, 0.023, and 0.015 min^{-1}, respectively, under visible light irradiation for 120 min (Fig. 3E). The degradation of high concentrations of TC produces a large number of intermediates, which compete with the parent molecules to occupy the active sites on catalyst surface, thus inhibiting its photocatalytic degradation efficiency. TC degradation can also be confirmed *via* its mineralization efficiency which is quantified by the TOC value (Fig. 3F). Catalyzed by the re-CuNiFe-MMOs, the decomposition efficiency of TC (50 mg L^{-1}) reaches 51.1% under visible light irradiation for 15 min (Fig. S15†), and the TOC value becomes 26.4%. When the TC degradation rate reaches 98.2% after 90 min, the TOC value becomes 70.2%, indicating that most of the TC has been degraded to CO_2 and H_2O, and only some is degraded into organic small molecule intermediates, which would be further degraded into harmless inorganic matter as the reaction continued. The above two values are much higher than 74.4% ($K = 0.0077$ min^{-1}) and 44.8% for the re-CuFe-MMOs, 62.1% ($K = 0.0038$ min^{-1}) and 40.5% for the re-CuNi-MMOs, and 51.3% ($K = 0.0035$ min^{-1}) and 37.7% for the re-FeNi-MMOs. Therefore, the synergistic effect of the photocatalysis and Fenton-like process could greatly promote the degradation of TC at a high concentration. This synergetic effect can also be demonstrated by testing the proliferation concentration of *E. coli.* As shown in Fig. 3G, living *E. coli* has a concentration of 17 500 cfu mL^{-1} in the original 50 mg L^{-1} TC solution, whereas the amount of *E. coli* within the degraded TC solution catalyzed by the re-CuNiFe-MMOs increased to ~52 000 000 cfu mL^{-1} after proliferation at 37 °C for 12 h, indicating that the TC concentration is degraded to less than 1 mg L^{-1}.
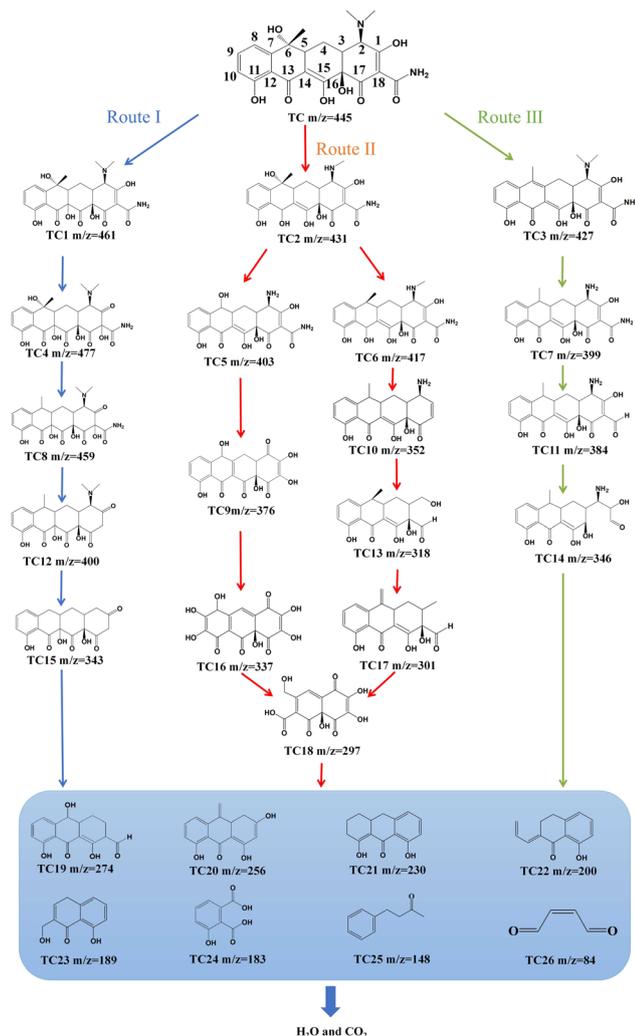
In addition, the universality of the re-CuNiFe-MMOs toward the catalytic degradation of chlortetracycline and oxytetracycline was further investigated. As expected, the re-CuNiFe-MMOs exhibits outstanding catalytic activities for oxidation of both CTC and OTC (10 mg L^{-1}), and the removal rates are 97.7% ($K = 0.57$ min^{-1}) and 93.3% (0.32 min^{-1}), respectively, in 10 min (Fig. 3H and Fig. S16†). All the above analysis results indicate that the re-CuNiFe-MMOs with multiple nanophases and stable 2D hetero-nanostructured clusters allow excellent

Fenton-like photocatalytic performance and reusability toward TC degradation, which creates great potential for their practical applications. Additionally, two kinds of non-tetracycline antibiotics, AMP and KAN, were selected to verify the universality of the degradation performance (Table S3 and Fig. S17†). The degradation rates of AMP and KAN at 10 mg L^{-1} under visible light are 97.8% (16 min, $K = 0.25$ min^{-1}) and 97.0% (20 min, $K = 0.18$ min^{-1}), respectively, further confirming that the re-CuNiFe-MMOs is universally applicable to the degradation of other types of antibiotics.

3.3. Intermediates and pathway of TC degradation

Based on above analysis, the re-CuNiFe-MMOs system enables the Fenton-like photocatalysis process to produce lots of $^{•}O_2^{-}$, causing the generation of a series of intermediates during the degradation of TC, which can be monitored by LC-MS. The MS's full scan mode was used to select the mass-to-charge ratio (m/z) values of the main intermediates, and the obtained results are shown in Fig. S18.† The possible molecular structures of the main intermediates are listed in Table S3.† The functional groups (*e.g.* amine groups, phenolic groups, and double bonds) of TC can be attacked by $^{•}O_2^{-}$and $^{•}OH$ due to their relatively high electron densities. Different types of intermediates (26 in total) can be monitored during the Fenton-like photocatalysis process for TC degradation. The loss of functional groups and ring opening reactions are the two main decomposition mechanisms of TC contributing to the phenomena of dehydroxylation, demethylation, hydroxylation, and amide bond cleavage.[16]

According to the above results, three possible TC degradation pathways were proposed, as shown in Fig. 4. For route I, the C14 and C15 double bonds with their highest electron density in TC are preferentially attacked by ROSs to generate primary intermediate TC1 ($m/z = 461$). Reactions with ROSs at the C1 and C18 double bonds of TC1 can produce intermediate TC4 ($m/z = 477$). TC4 undergoes a dehydroxylation reaction at position C6 to form TC8 ($m/z = 459$), followed by a deamidation reaction at position C18 to generate TC12 ($m/z = 400$). TC15 ($m/z = 343$) is also produced after the removal of the amino and methyl groups of TC12 at positions C2 and C6, respectively. For route II, the TC molecule is converted to TC2 ($m/z = 431$) because of the demethylation process at position C2. Then, demethylation at positions C2 and C6 and dehydroxylation reaction at position C13 of TC2 produce TC5 ($m/z = 403$). Subsequently, TC5 can undergo a series of processes of deamination, dehydrogenation, and amide bond cleavage, at positions C2, C14 and C15, and C18, respectively, resulting in the formation of TC9 ($m/z = 376$). Then, TC9 undergoes dehydrogenation at positions C3 and C4, and is further degraded by oxidative reactions, undergoing loop opening and hydroxylation at C7 and C12 to generate TC16 ($m/z = 337$). After that, due to the unstable structure of the enol form in TC16, it is transformed into the ketone form,[34] and a ring-opening reaction occurs to produce TC18 ($m/z = 297$).[16] Simultaneously, the dehydroxylation reaction of TC2 occurs at position C6 to form TC6 ($m/z = 417$). The $^{•}OH$ radical can attack positions C1, C2,
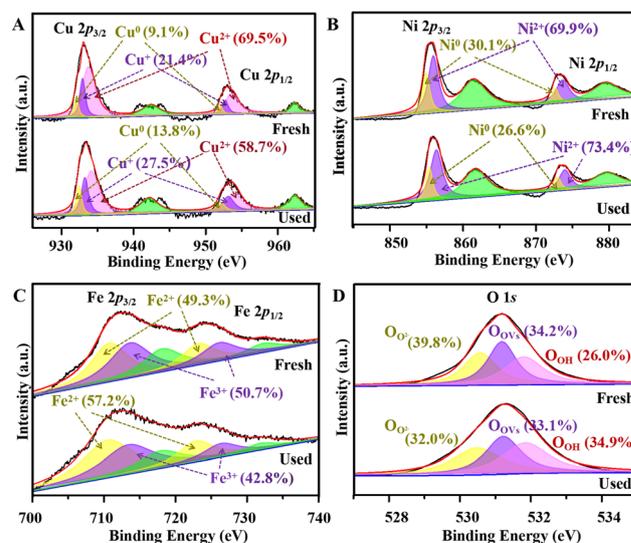
572 | *Inorg. Chem. Front.*, 2023, **10**, 567–578

This journal is © the Partner Organisations 2023

Fig. 4 The pathways for TC degradation in the re-CuNiFe-MMOs system under visible light irradiation.

molecules with m/z values of 274, 256, 230, 200, 189, 183, 148 and 84 through a series of dissociation and ring-opening processes. Finally, the above products are mineralized into harmless inorganic substances by the generated ROSs in the reaction system, and the TC structure is completely destroyed.

3.4. Catalytic reaction mechanism

Further analysis was carried out to reveal the catalytic mechanisms for TC degradation. First, XPS spectra were compared for the fresh and used re-CuNiFe-MMOs (Fig. 5). As expected, Cu, Fe, Ni, and O can be clearly detected in the survey spectra (Fig. S19†). The high-resolution spectrum of Cu 2p has two strong peaks at 933.1 and 952.9 eV for spin orbits of Cu 2p 1/2 and Cu 2p 3/2, which can be decomposed into three pairs of peaks, *i.e.* 932.1 and 952.1 eV, 933.0 and 952.8 eV, and 933.7 and 953.7 eV, corresponding to Cu^0, Cu^+ and Cu^{2+}, respectively (Fig. 5A).[35] After application to degrade TC, in the fresh and used re-CuNiFe-MMOs, the percentage of Cu^{2+} decreased significantly from 69.5% to 58.7%, whereas the percentages of Cu^+ and Cu^0 increased from 21.4% to 27.5%, and 9.1% to 13.8%, respectively. For Ni 2p, the peaks of Ni 2p3/2 and Ni 2p1/2 can be divided into two pairs of peaks, *i.e.* 855.0 and 872.8 eV, and 856.0 and 873.7 eV (Fig. 5B). They can be assigned to Ni^0 and Ni^{2+}, respectively, corresponding to CuNi and NiO. Comparing before and after use in the catalytic reaction, the percentage of Ni^0 decreased from 30.1% to 26.6%, while the percentage of Ni^{2+} increased from 69.9% to 73.4%. For Fe 2p, two strong peaks at 712.1 (Fe 2p 3/2) and 723.8 eV (Fe 2p 1/2) can be divided into two pairs of peaks at 710.7 and 723.2 eV, and 713.7 and 726.2 eV, corresponding to Fe^{2+} and Fe^{3+}, respectively (Fig. 5C).[16] The percentage of Fe^{2+} in the used sample is increased significantly from 49.3% to 57.2%, accompanied by a decrease of Fe^{3+} content from 50.7% to 42.8%. In brief, XPS analysis shows that during the Fenton-like

C13 and C18, TC6 to form TC10 (m/z = 352) through dehydroxylation and deamination reaction. Then, due to the attack of ˙OH radicals, the deamination reactions at position C2 and the cleavage of the C1 and C18 double bonds of TC10 generate TC13 (m/z = 318). Further dehydroxylation and demethylation reactions at positions C2 and C6 of TC13 produce TC17 (m/z = 301). This TC17 undergoes demethylation, hydroxylation, ketonization, double bond cleavage, ring-opening reaction and dialdehyde reaction at positions C3, C4, C6, C8, C11, and C16, respectively, to form TC18 (m/z = 297). For route III, hydrogen and hydroxyl at positions C5 and C6 on TC are dehydrated and converted into anhydrous tetracycline TC3 (m/z = 427). Through TC3 demethylation in the amino group at position C2, TC7 (m/z = 399) appears. The amide at position C18 of TC6 is attacked by free radicals, and is further deaminated and converted into TC11 (m/z = 384). Then, TC11 undergoes a ring-opening reaction at C18, resulting in the formation of TC14 (m/z = 346). As the degradation reaction is further progressed, these intermediates are further oxidized into organic small

Fig. 5 The detailed XPS survey spectra analysis of Cu 2p (A), Fe 2p (B), Ni 2p (C) and O 1s (D) for the fresh and used re-CuFeNi-MMOs catalyst.

This journal is © the Partner Organisations 2023

Inorg. Chem. Front., 2023, **10**, 567–578 | **573**

photocatalytic degradation of TC by the re-CuNiFe-MMOs, an increased proportion of high-valence Cu^{2+} and Fe^{3+} is partially converted to Cu^+ and Fe^{2+}, which demonstrates that changes in Fe(II)–Fe(III) and Cu(I)–Cu(II) occur during the radical generation.[2] Additionally, there are three deconvoluted O 1s peaks at 530.6, 531.2 and 531.8 eV corresponding to lattice oxygen, defect oxygen and hydroxyl oxygen, respectively (Fig. 5D).[36] The degradation reaction causes the proportions of lattice and defect oxygen to decrease from 39.8% to 32.0% and 34.2% to 33.1%, respectively, due to their activation for the dissolved oxygen,[37] while the proportion of hydroxyl oxygen is increased from 26.0% to 34.9% because of the attachment of constantly generated OH^- on the surface of the re-CuNiFe-MMOs.

Next, the optical absorption properties of the samples were analyzed by UV-vis DRS. In Fig. 6A, owing to the multiple valence of Cu, the re-CuNiFe-MMOs, re-CuFe-MMOs, and re-CuNi-MMOs all exhibit strong light absorption capabilities, which are mainly due to the excitation transition of Cu $3d^9$ from $d_{x^2-y^2}$ to d_{xy}. Meanwhile, iron oxides containing samples of the re-CuNiFe-MMOs, re-CuFe-MMOs, and re-FeNi-MMOs show red shifts. According to the relationship between the tangent of $(\alpha h\nu)^2$ and the energy $(h\nu)$,[38] the corresponding bandgap energies (E_g) of the re-CuNiFe-MMOs, re-CuFe-MMOs, re-CuNi-MMOs and re-FeNi-MMOs were calculated to be 1.63, 1.71, 1.85 and 1.99 eV, respectively (Fig. 6B). These data agree well with the values calculated using the formula E_g (eV) = 1240 λ^{-1} (where λ is the wavelength of maximum absorption). Since the band structure determines the generation and migration of the photogenerated carriers, the valence band positions (E_{VB}) were studied by using VB-XPS (Fig. 6C). The E_{VB}

values of the re-CuNiFe-MMOs, re-CuFe-MMOs, re-CuNi-MMOs, and re-FeNi-MMOs are 0.54, 1.08, 1.25, and 1.32 eV, respectively. Their corresponding conduction band edge potentials (E_{CB}) are calculated to be −1.09, −0.63, −0.60 and −0.67 eV, respectively, according to the equation $E_{CB} = E_{VB} - E_g$. Because the E_{CB} value is more negative than the potential of $O_2/{\cdot}O_2^-$ (−0.33 eV vs. NHE), the dissolved O_2 in the solution can be converted to ${\cdot}O_2^-$ by the activation of conduction band electrons. Hence, the re-CuNiFe-MMOs has the highest negative value for E_{CB}, and is the most efficient to produce ${\cdot}O_2^-$ for high catalytic activity.

The separation capabilities of the photogenerated e^-/h^+ pairs were further investigated by employing PL, photocurrent, and EIS analysis. The PL intensity is significantly influenced by the photocatalytic activity, since its emission signal is derived from the energy released by the recombination of carriers.[16] Fig. 6D presents the emission spectra of the prepared samples under an excitation wavelength of 350 nm. A strong emission peak at 430 nm can be observed and the emission peak intensity order for the prepared catalysts is re-FeNi-MMOs > re-CuNi-MMOs > re-CuFe-MMOs > re-CuNiFe-MMOs. The re-CuNiFe-MMOs having the smallest emission peak intensity clearly indicates that it has the best separation efficiency for the photoexcited carriers. The separation efficiency of the photogenerated e^-/h^+ pairs can be revealed by transient photocurrent responses and the impedance technique. Generally, the stronger the photocurrent responses, or the smaller the impedance, the more effectively the photogenerated electrons and holes can be separated, which leads to a higher photocatalytic activity. Fig. 6E clearly illustrates that the
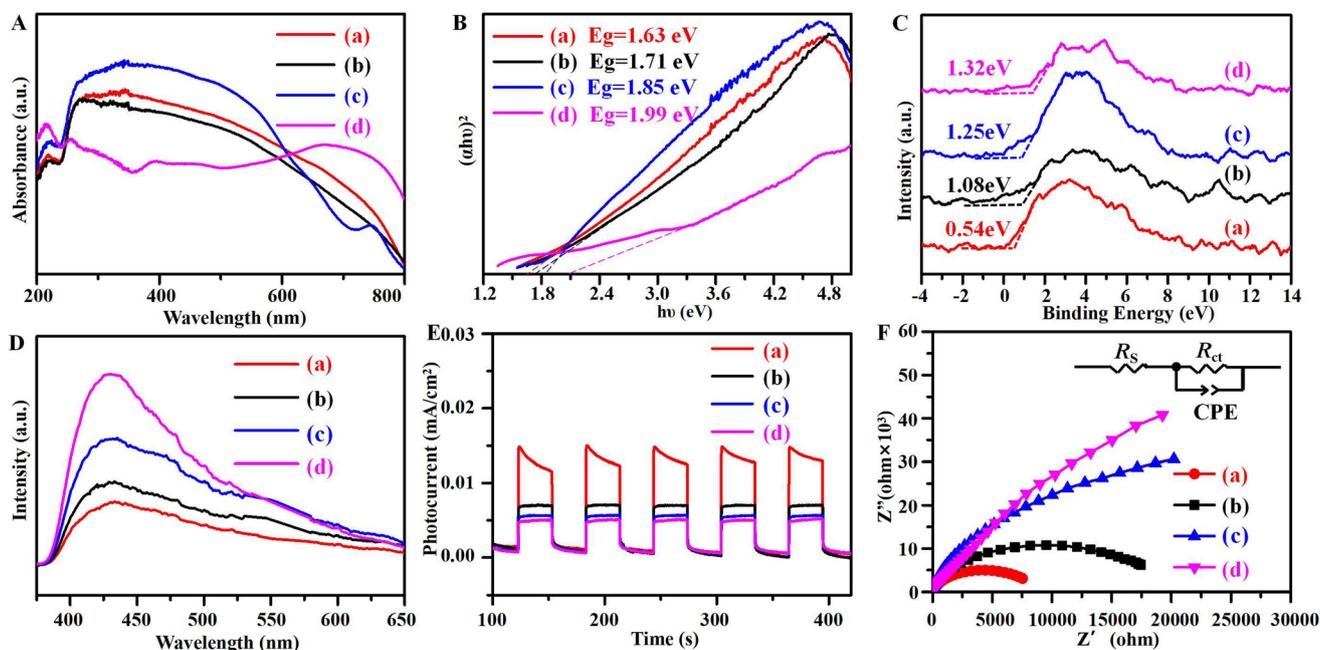

Fig. 6 (A) UV-vis DRS spectra, (B) Tauc plots, (C) VB-XPS spectra, (D) PL spectra, (E) transient photocurrent curves, and (F) Nyquist plots for EIS for the prepared samples. ((a) re-CuNiFe-MMOs, (b) re-CuFe-MMOs, (c) re-CuNi-MMOs, (d) re-FeNi-MMOs).

574 | *Inorg. Chem. Front.*, 2023, **10**, 567–578

This journal is © the Partner Organisations 2023

re-CuNiFe-MMOs has the highest photocurrent density. The EIS Nyquist curve of the re-CuNiFe-MMOs in Fig. 6F plots the minimum impedance to transfer electrons, and the corresponding equivalent circuit diagram is given in the inset.

Additionally, radical trapping experiments were carried out to prove the identity of the active species produced during the oxidative degradation on the photocatalyst surface.[39] Triethanolamine, *tert*-butanol (TBA), *p*-benzoquinone and furfuryl alcohol were selected as the probe reagents to quench h^+, $^\bullet OH$, $^\bullet O_2^-$ and $^1O_2$ radicals, respectively. As depicted in Fig. 7A and Fig. S20A,† the addition of TBA, FFA, TEA and BQ decrease the degradation rates of TC from 99.9% to 87.4%, 42.0%, 23.6% and 8.1%, respectively, whereas almost all the TC can be degraded if the scavenger is absent. This indicates that $^\bullet O_2^-$ radicals contribute to the photocatalytic reaction, which can be confirmed by carrying out the scavenging experiments under anaerobic conditions (Fig. S20B†). Compared with that of only 6.7% without any scavenger, the TC degradation rates are only 3.4%, 4.5%, 6.0% and 5.3% after trapping $^\bullet O_2^-$, h^+, $^\bullet OH$ and $^1O_2$ with BQ, TBA, TEA and FFA, *i.e.* almost unchanged. In comparison with the results of the re-CuFe-MMOs, re-CuNi-MMOs, and re-FeNi-MMOs, the re-CuNiFe-MMOs shows the highest catalytic degradation efficiency and is strongly affected by the trapping reagents, due to the numerous generated active species. The radical trapping experiments for CTC and OTC clearly show that $^\bullet O_2^-$ plays a key role in the photocatalytic degradation reaction of TCs in the re-CuNiFe-

MMOs catalysis system. In addition, the capture experiment was carried out under aerobic and anaerobic conditions in the dark (Fig. S21†). The results confirmed that the main active oxygen species to degrade TC is $^\bullet O_2^-$ under dark conditions.

To gain further insight into the effects of defects (*e.g.* OVs) on the catalyst, EPR tests were performed (Fig. 7B and Fig. S22†). The EPR line widths of the prepared samples are broadened due to the generated copper oxide (Cu–O) or ferrite oxide (Fe–O) vacancies. Both the re-CuNiFe-MMOs and re-CuFe-MMOs show higher and broader signal intensities with g ($h\gamma/\mu_B B$) of 2.0025–2.0060 than the re-CuNi-MMOs and re-FeNi-MMOs with g of 2.0035–2.0055. This is mainly due to the larger number of defects caused by the multiple oxidation states of Cu and Fe. The vacancy defects can promote charge separation and can be transformed into reactive species, thus leading to the enhanced Fenton-like photocatalytic activity. The generation of active species is further proved by EPR using DMPO and TEMP as spin-trapping reagents (Fig. 7C–E).[40] The signal intensities of $^\bullet O_2^-$, $^\bullet OH$ and $^1O_2$ are clearly increased with reaction times prolonged from 0 to 4 min under visible light. A similar trend can be observed when the Fenton-like reactions progressed from 0 to 45 min under dark conditions, although the signals are much weaker. The intensity attenuation of these signals can be observed to be in the order re-CuNiFe-MMOs < re-CuFe-MMOs < re-CuNi-MMOs < re-FeNi-MMOs under the same irradiation time (Fig. S23†), confirming that the re-CuNiFe-MMOs can produce the largest number of
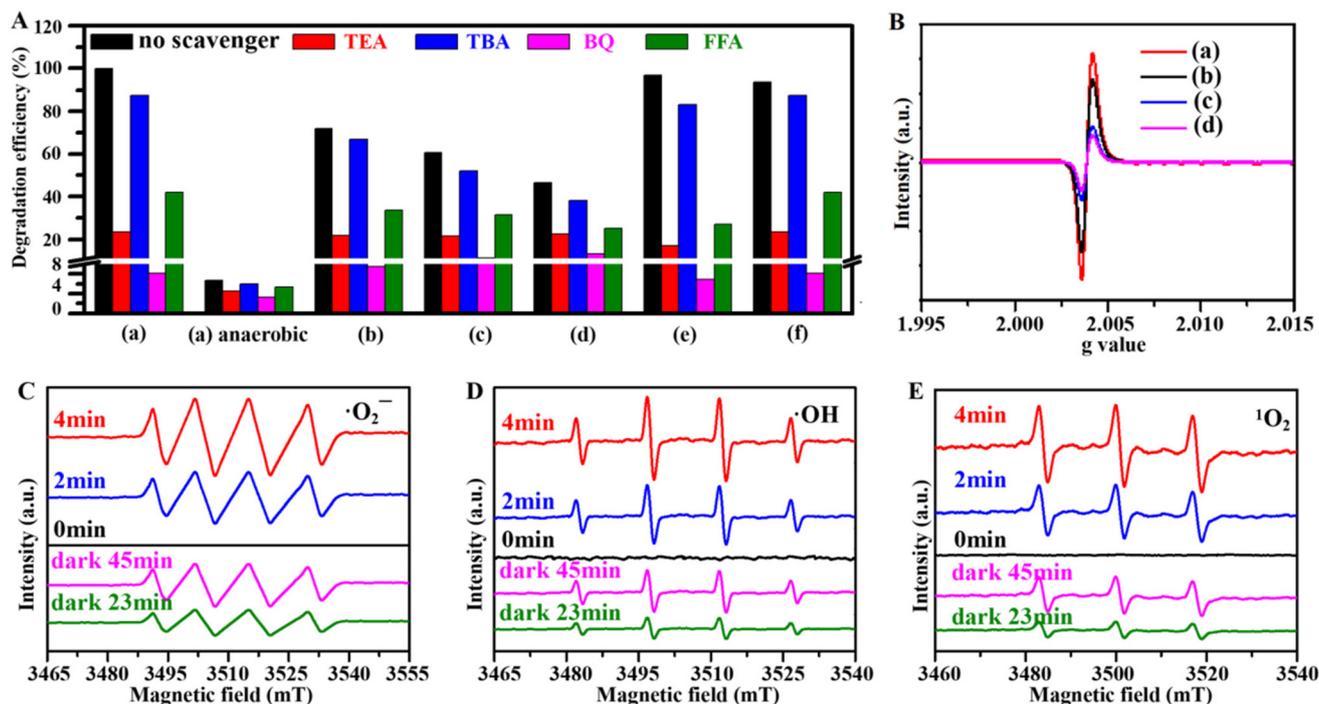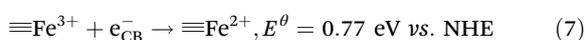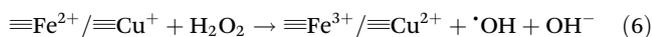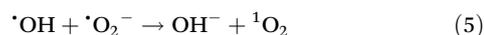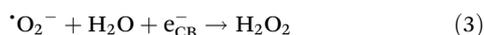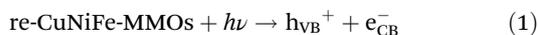

Fig. 7 (A) The effect of radical scavengers on the degradation of TC by the prepared catalysts under aerobic and anaerobic conditions under visible light irradiation. (B) EPR patterns of the prepared catalysts. (C–E) EPR spectra of $^\bullet O_2^-$, $^\bullet OH$, and $^1O_2$ using the re-CuNiFe-MMOs under visible light and in the dark at different reaction times. ((a) re-CuNiFe-MMOs, (b) re-CuFe-MMOs, (c) re-CuNi-MMOs, (d) re-FeNi-MMOs, (e) CTC, (f) OTC). (Operating parameters: 0.25 g L^{-1} catalyst, 25 °C, 10 mg L^{-1} TC, pH 7.2).

active species in the reaction process, thus showing the best TC degradation performance.
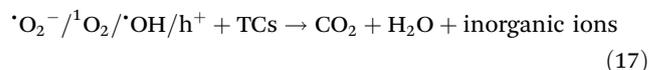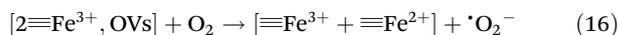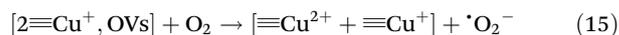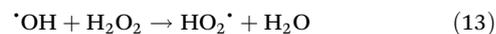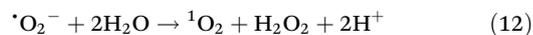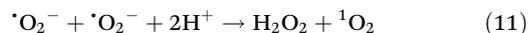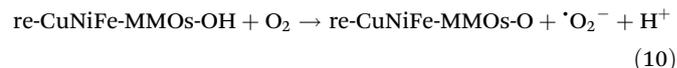
3.5. Fenton-like photocatalytic enhancement mechanism

Based on the above analysis, a Fenton-like photocatalytic enhancement mechanism can be proposed for the efficient degradation of TCs in the re-CuNiFe-MMOs system under visible light irradiation, and is illustrated in Fig. 1B. The photogenerated electrons e^- from the valence band (VB) easily migrate to the conduction band (CB) at a relatively low potential, thus leaving a lot of holes in the VB (eqn (1)). Then, those electrons e_{CB}^- are transferred by the CuNi nanophases immediately, and are captured by O_2 on the surface of the catalyst. They can form the main source to provide $^\bullet O_2^-$, which promotes the migration and reaction of photogenerated electrons, thus accelerating the separation of the carriers (eqn (2)). Since the negative potential of the CB (-1.09 eV) of the re-CuNiFe-MMOs is much lower than the standard reduction potential of O_2 ($E^\theta(O_2/^\bullet O_2^-) = -0.33$ eV $vs.$ NHE),[41] the electrons trapped in the CB can be rapidly reduced by the dissolved oxygen to $^\bullet O_2^-$, which then forms H_2O_2 by reacting with e_{CB}^- and H_2O (eqn (3)).[42] The $^\bullet OH$ generated by e_{CB}^- and H_2O_2 (eqn (4)) then reacts with $^\bullet O_2^-$ to produce $^1O_2$ (eqn (5)). The VB holes with a potential of 0.54 eV are insufficient to oxidize surface-adsorbed H_2O and OH^- to generate $^\bullet OH$ ((E^θ ($H_2O/^\bullet OH$) = 2.38 eV $vs.$ NHE, E^θ ($OH^-/^\bullet OH$) = 1.99 eV $vs.$ NHE).[43] These separated holes are directly involved in the catalytic oxidation of the TC. For the re-CuNiFe-MMOs, the interfacial electron transfer can be significantly improved due to the redox cycles of Fe^{3+}/Fe^{2+} and Cu^{2+}/Cu^+, and the regenerated Fe^{2+} and Cu^+ significantly enhance the TC degradation. The standard reduction potential of Cu^{2+}/Cu^+ is 0.17 eV and that of Fe^{3+}/Fe^{2+} is 0.77 eV, so Cu^+ can reduce Fe^{3+} via thermodynamically favorable electron transfer (eqn (6)–(9)).

$$re\text{-}CuNiFe\text{-}MMOs + h\nu \rightarrow h_{VB}^+ + e_{CB}^- \tag{1}$$

$$O_2 + e_{CB}^- \rightarrow {}^\bullet O_2^- \tag{2}$$

$$^\bullet O_2^- + H_2O + e_{CB}^- \rightarrow H_2O_2 \tag{3}$$

$$e_{CB}^- + H_2O_2 \rightarrow {}^\bullet OH + OH^- \tag{4}$$

$$^\bullet OH + {}^\bullet O_2^- \rightarrow OH^- + {}^1O_2 \tag{5}$$

$$\equiv Fe^{2+}/\equiv Cu^+ + H_2O_2 \rightarrow \equiv Fe^{3+}/\equiv Cu^{2+} + {}^\bullet OH + OH^- \tag{6}$$

$$\equiv Fe^{3+} + e_{CB}^- \rightarrow \equiv Fe^{2+}, E^\theta = 0.77 \text{ eV } vs. \text{ NHE} \tag{7}$$

$$\equiv Cu^{2+} + e_{CB}^- \rightarrow \equiv Cu^+, E^\theta = 0.17 \text{ eV } vs. \text{ NHE} \tag{8}$$

$$\equiv Fe^{3+} + \equiv Cu^+ \rightarrow \equiv Cu^{2+} + \equiv Fe^{2+} \tag{9}$$
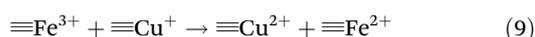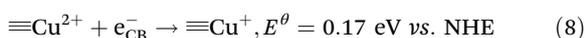
The polyols act as a reductant in the catalyst preparation process, which can afford abundant –OH attached on the surface of the re-CuNiFe-MMOs. This has been verified by the IR results (Fig. S24†). The –OH groups act as electron donors for the TC degradation, and the corresponding mechanism of O_2 activation is shown in eqn (10) and (11). According to eqn (12)–(14), a secondary reactive species generated by $^\bullet O_2^-$

($e.g.$ $^\bullet OH$ and $^1O_2$) then participates in the oxidative degradation processes as shown by the following equations.

$$re\text{-}CuNiFe\text{-}MMOs\text{-}OH + O_2 \rightarrow re\text{-}CuNiFe\text{-}MMOs\text{-}O + {}^\bullet O_2^- + H^+ \tag{10}$$

$$^\bullet O_2^- + {}^\bullet O_2^- + 2H^+ \rightarrow H_2O_2 + {}^1O_2 \tag{11}$$

$$^\bullet O_2^- + 2H_2O \rightarrow {}^1O_2 + H_2O_2 + 2H^+ \tag{12}$$

$$^\bullet OH + H_2O_2 \rightarrow HO_2^\bullet + H_2O \tag{13}$$

$$HO_2^\bullet \rightarrow H^+ + {}^\bullet O_2^- \tag{14}$$

$$[2\equiv Cu^+, OVs] + O_2 \rightarrow [\equiv Cu^{2+} + \equiv Cu^+] + {}^\bullet O_2^- \tag{15}$$

$$[2\equiv Fe^{3+}, OVs] + O_2 \rightarrow [\equiv Fe^{3+} + \equiv Fe^{2+}] + {}^\bullet O_2^- \tag{16}$$

$$^\bullet O_2^-/{}^1O_2/{}^\bullet OH/h^+ + TCs \rightarrow CO_2 + H_2O + \text{inorganic ions} \tag{17}$$

In the Fenton-like photocatalytic degradation process, the OVs formed by the $in\ situ$ reduction of the CuNiFe-MMOs can adsorb O_2 and produce $^\bullet O_2^-$ (eqn (15) and (16)). Ultimately, TC on the catalyst surface is efficiently decomposed into CO_2, H_2O and other inorganic small molecules by all the ROSs formed in the system (eqn (17)). In brief, the large specific surface area, exposed active sites, tunable band gaps, valence changes of Cu and Fe, and abundant defects ($e.g.$ OVs) are the key factors meaning that the re-CuNiFe-MMOs system has excellent catalytic activity for TC degradation.

4. Conclusions

A cluster-structure assembled by re-CuNiFe-MMOs nanosheets has been integrated into the HPSR process for TC degradation. Attributed to the 2D structured multiple nanophases of the alloy and MMOs with multivalent Cu ions, a large specific surface area and numerous exposed active sites have been created. These 2D heterostructured clusters provide efficient mass transfer. The interfaces of multiple nanophases form abundant defects ($e.g.$ OVs) and produce active radicals ($^\bullet O_2^-$, $^1O_2$, $^\bullet OH$ and h^+). Therefore, the as-obtained re-CuNiFe-MMOs efficiently degrades TCs through Fenton-like photocatalysis without using any additional oxidants. This work provides a green method for highly efficient Fenton-like photocatalysis for TC degradation.

Author contributions

Lin Fu: investigation, writing – original draft. Dandan Wu: investigation, analysis, writing – original draft. Ming Wen: supervision, conceptualization, methodology, validation, writing – review and editing. Yuanzheng Zhu: writing – review and editing. Qingsheng Wu: writing – review and editing. Tao Zhou: writing -–review and editing. Yongqing Fu: writing – review and editing.

Conflicts of interest

There are no conflicts to declare.

Acknowledgements

References

1 Z. L. Li, C. S. Guo, J. C. Lu, Z. Hu and M. Ge, Tetracycline degradation by persulfate activated with magnetic Cu/ $CuFe_2O_4$ composite: Efficiency, stability, mechanism and degradation pathway, *J. Hazard. Mater.*, 2019, **373**, 85–96.

2 J. Yu, J. Kiwi, I. Zivkovic, H. M. Rønnow, T. Wang and S. Rtimi, Quantification of the local magnetized nanotube domains accelerating the photocatalytic removal of the emerging pollutant tetracycline, *Appl. Catal., B*, 2019, **248**, 450–458.

3 F. B. Yin, H. M. Dong, W. Q. Zhang, Z. P. Zhu and B. Shang, Antibiotic degradation and microbial community structures during acidification and methanogenesis of swine manure containing chlortetracycline or oxytetracycline, *Bioresour. Technol.*, 2018, **250**, 247–255.

4 T. Kaeseberg, J. Zhang, S. Schubert, R. Oertel and P. Krebs, Abiotic, biotic and photolytic degradation affinity of 14 antibiotics and one metabolite e batch experiments and a model framework, *Environ. Pollut.*, 2018, **241**, 339–350.

5 S. Han and P. Xiao, Catalytic degradation of tetracycline using peroxymonosulfate activated by cobalt and iron co-loaded pomelo peel biochar nanocomposite: Characterization, performance and reaction mechanism, *Sep. Purif. Technol.*, 2022, **287**, 120533.

6 C. Wang, R. Sun, R. Huang and H. Wang, Superior fenton-like degradation of tetracycline by iron loaded graphitic carbon derived from microplastics: Synthesis, catalytic performance, and mechanism, *Sep. Purif. Technol.*, 2021, **270**, 118773.

7 W. Ding, X. Huang, W. Zhang, F. Wu and J. Li, Sulfite activation by a low-leaching silica-supported copper catalyst for oxidation of As(III) in water at circumneutral pH, *Chem. Eng. J.*, 2019, **359**, 1518–1526.

8 Y. Gan, Y. Wei, J. Xiong and G. Cheng, Impact of post-processing modes of precursor on adsorption and photocatalytic capability of mesoporous TiO_2 nanocrystallite aggregates towards ciprofloxacin removal, *Chem. Eng. J.*, 2018, **349**, 1–16.

9 W. K. Jo and T. S. Natarajan, Facile Synthesis of Novel Redox-Mediator-free Direct Z-Scheme $CaIn_2S_4$ Marigold-Flower-like/TiO_2 Photocatalysts with Superior Photocatalytic Efficiency, *ACS Appl. Mater. Interfaces*, 2015, **7**(31), 17138–17154.

10 A. Serrà, R. Artal, J. García-Amorós, E. Gómez and L. Philippe, Circular zero-residue process using microalgae for efficient water decontamination, biofuel production, and carbon dioxide fixation, *Chem. Eng. J.*, 2020, **388**, 124278.

11 H. Qin, H. Cheng, H. Li and Y. Wang, Degradation of ofloxacin, amoxicillin and tetracycline antibiotics using magnetic core–shell $MnFe_2O_4$@$C-NH_2$ as a heterogeneous Fenton catalyst, *Chem. Eng. J.*, 2020, **396**, 125304.

12 J. Liu, K. Luo, X. M. Li, Q. Yang, D. B. Wang, Y. Wu, Z. Chen, X. D. Huang, Z. J. Pi, W. J. Du and Z. L. Guan, The biochar-supported iron-copper bimetallic composite activating oxygen system for simultaneous adsorption and degradation of tetracycline, *Chem. Eng. J.*, 2020, **402**, 12603.

13 H. Zhang, Y. Y. Song, L. C. Nengzi, J. F. Gou, B. Li and X. W. Cheng, Activation of persulfate by a novel magnetic $CuFe_2O_4$/Bi_2O_3 composite for lomefloxacin degradation, *Chem. Eng. J.*, 2020, **379**, 122362.

14 X. L. Zhu, H. H. Miao, J. Z. Chen, X. W. Zhu, J. J. Yi, Z. Mo, H. M. Li, Z. K. Zheng, B. B. Huang and H. Xu, Facet-dependent CdS/Bi_4TaO_8Cl Z-scheme heterojunction for enhanced photocatalytic tetracycline hydrochloride degradation and the carrier separation mechanism study via single-particle spectroscopy, *Inorg. Chem. Front.*, 2022, **9**, 2252–2263.

15 S. J. Li, M. J. Cai, Y. P. Liu, J. L. Zhang, C. C. Wang, S. H. Zang, Y. J. Li, P. Zhang and X. Li, In situ construction of a C_3N_5 nanosheet/Bi_2WO_6 nanodot S-scheme heterojunction with enhanced structural defects for the efficient photocatalytic removal of tetracycline and Cr(VI), *Inorg. Chem. Front.*, 2022, **9**, 2479–2497.

16 A. Wang, Z. K. Zheng, H. Wang, Y. W. Chen, C. H. Luo, D. J. Liang, B. Hu, R. L. Qiu and K. Yan, 3D hierarchical H_2-reduced Mn-doped CeO_2 microflowers assembled from nanotubes as a high-performance Fenton-like photocatalyst for tetracycline antibiotics degradation, *Appl. Catal., B*, 2020, **277**, 119171.

17 H. C. Shan, D. Cai, X. X. Zhang, Q. Zhu, P. Y. Qin and J. Baeyens, Donor-acceptor type two-dimensional porphyrin-based covalent organic framework for visible-light-driven heterogeneous photocatalysis, *Chem. Eng. J.*, 2022, **432**, 134288.

18 G. T. Zan, T. Wu, F. Zhu, P. F. He, Y. P. Cheng, S. S. Chai, Y. Wang, X. F. Huang, W. X. Zhang, Y. Wan, X. J. Peng and Q. S. Wu, A Biomimetic Conductive Super-foldable Material, *Matter*, 2021, **4**(10), 3232–3247.

19 S. S. Chai, G. T. Zan, K. Z. Dong, T. Wu and Q. S. Wu, Approaching Superfoldable Thickness-Limit Carbon Nanofiber Membranes Transformed From Water-Soluble PVA, *Nano Lett.*, 2021, **21**, 8831–8838.

20 Z. F. Yang, X. N. Xia, L. H. Shao, L. L. Wang and Y. T. Liu, Efficient photocatalytic degradation of tetracycline under

This journal is © the Partner Organisations 2023

Inorg. Chem. Front., 2023, **10**, 567–578 | 577

visible light by Z-scheme Ag_3PO_4/mixed-valence MIL-88A (Fe) heterojunctions: Mechanism insight, degradation pathways and DFT calculation, *Chem. Eng. J.*, 2021, **410**, 128454.

21 Y. Y. Liu, X. J. Wang, Q. N. Sun, M. Yuan, Z. H. Sun, S. Q. Xia and J. F. Zhao, Enhanced visible light photo-Fenton-like degradation of tetracyclines by expanded perlite supported $FeMo_3O_x$/g-C_3N_4 floating Z-scheme catalyst, *J. Hazard. Mater.*, 2022, **424**, 127387.

22 G. T. Zan, T. Wu, Z. L. Zhang, J. Li, J. C. Zhou, F. Zhu, H. X. Chen, M. Wen, X. Yang, X. Peng, J. Chen and Q. Wu, Bioinspired Nanocomposites with Self-adaptive Stress Dispersion for Super-Foldable Electrodes, *Adv. Sci.*, 2022, **9**(3), 2103714.

23 G. T. Zan, T. Wu, W. Y. Dong, J. C. Zhou, T. Tu, R. X. Xu, Y. Chen, Y. Wang and Q. S. Wu, Two-Level Biomimetic Designs Enable Intelligent Stress Dispersion for Super-Foldable C/NiS Nanofiber Free-Standing Electrode, *Adv. Fiber Mater.*, 2022, **4**, 1177–1190.

24 R. Hailili, Z. Q. Wang, X. Q. Gong and C. Y. Wang, Oxygen vacancies induced visible-light photocatalytic activities of $CaCu_3Ti_4O_{12}$ with controllable morphologies for antibiotic degradation, *Appl. Catal., B*, 2018, **221**, 422–432.

25 L. Fu, W. Zhou, M. Wen and D. D. Wu, Layered CuNi-Cu_2O/NiAlO$_x$ nanocatalyst for rapid conversion of p-nitrophenol to p-aminophenol, *Nano Res.*, 2021, **14**(12), 4616–4624.

26 F. Wu, S. Banerjee, H. F. Li, Y. Myung and P. Banerjee, Indirect Phase Transformation of CuO to Cu_2O on a Nanowire Surface, *Langmuir*, 2016, **32**, 4485–4493.

27 A. I. Kontos, V. Likodimos, T. Stergiopoulos, D. S. Tsoukleris and P. Falaras, Self-Organized Anodic TiO_2 Nanotube Arrays Functionalized by Iron Oxide Nanoparticles, *Chem. Mater.*, 2009, **21**, 662–672.

28 T. Vandhana and A. J. C. Lourduraj, Biogenic synthesis of Mn-Ag co-doped FeO ($Fe_{1-2x}Mn_xAg_x$) nanoparticles: As an effective disinfectant and anticancer agent, *Inorg. Chem. Commun.*, 2020, **112**, 107712.

29 H. Naatz, S. Lin, R. B. Li, W. Jiang, Z. X. Ji, C. H. Chang, J. Koser, T. Xia, A. E. Nel, L. Madler and S. Pokhrel, Safe-by-Design CuO Nanoparticles via Fe-Doping, Cu–O Bond Length Variation, and Biological Assessment in Cells and Zebrafish Embryos, *ACS Nano*, 2017, **11**, 501–515.

30 L. Zhang, Y. Nie, C. Hu and J. Qu, Enhanced Fenton degradation of Rhodamine B over nanoscaled Cu-doped $LaTiO_3$ perovskite, *Appl. Catal., B*, 2012, **125**, 418–424.

31 Y. Wang, H. Zhao and G. Zhao, Iron-copper bimetallic nanoparticles embedded within ordered mesoporous carbon as effective and stable heterogeneous Fenton catalyst for the degradation of organic contaminants, *Appl. Catal., B*, 2015, **164**, 396–406.

32 X. Dong, B. Ren, Z. Sun, C. Li, X. Zhang, M. Kong, S. Zheng and D. D. Dionysiou, Monodispersed $CuFe_2O_4$ nanoparticles anchored on natural kaolinite as highly efficient peroxymonosulfate catalyst for Bisphenol A degradation, *Appl. Catal., B*, 2019, **253**, 206–217.

33 X. Zhang, Y. Ding, H. Tang, X. Han, L. Zhu and N. Wang, Degradation of bisphenol A by hydrogen peroxide activated with $CuFeO_2$ microparticles as a heterogeneous Fenton-like catalyst: Efficiency, stability and mechanism, *Chem. Eng. J.*, 2014, **236**, 251–262.

34 J. Zhou, F. Ma, H. Guo and D. Su, Activate hydrogen peroxide for efficient tetracycline degradation via a facile assembled carbon-based composite: Synergism of powdered activated carbon and ferroferric oxide nanocatalyst, *Appl. Catal., B*, 2020, **269**, 118784.

35 S. Chen, L. Tang, H. Feng, Y. Zhou, G. Zeng, Y. Lu, J. Yu, X. Ren, B. Peng and X. Liu, Carbon felt cathodes for electro-Fenton process to remove tetracycline via synergistic adsorption and degradation, *Sci. Total Environ.*, 2019, **670**, 921–931.

36 H. Zheng, J. Bao, Y. Huang, L. Xiang, B. Faheem, J. Ren, M. N. Du and D. D. D. Nadagouda, Efficient degradation of atrazine with porous sulfurized Fe_2O_3 as catalyst for peroxymonosulfate activation, *Appl. Catal., B*, 2019, **259**, 118056.

37 W. Zhou, L. Fu, L. Zhao, X. Xu, W. Li, M. Wen and Q. Wu, Novel Core–Sheath Cu/Cu_2O-ZnO-Fe_3O_4 Nanocomposites with High-Efficiency Chlorine-Resistant Bacteria Sterilization and Trichloroacetic Acid Degradation Performance, *ACS Appl. Mater. Interfaces*, 2021, **13**, 10878–10890.

38 X. F. Wei, H. Feng, L. W. Li, J. B. Gong, K. Jiang, S. L. Xue and P. K. Chu, Synthesis of tetragonal prismatic γ-In_2Se_3 nanostructures with predominantly {110} facets and photocatalytic degradation of tetracycline, *Appl. Catal., B*, 2020, **260**, 118218.

39 S. Adhikari, S. Mandal and D. H. Kim, Z-scheme 2D/1D MoS_2 nanosheet-decorated $Ag_2Mo_2O_7$ microrods for efficient catalytic oxidation of levofloxacin, *Chem. Eng. J.*, 2019, **373**, 31–43.

40 S. Adhikari, H. H. Lee and D. H. Kim, Efficient visible-light induced electron-transfer in Z-scheme MoO_3/Ag/C_3N_4 for excellent photocatalytic removal of antibiotics of both ofloxacin and tetracycline, *Chem. Eng. J.*, 2020, **391**, 123504.

41 B. Wang, J. Di, P. Zhang, J. Xia, S. Dai and H. Li, Ionic liquid-induced strategy for porous perovskite-like $PbBiO_2Br$ photocatalysts with enhanced photocatalytic activity and mechanism insight, *Appl. Catal., B*, 2017, **206**, 127–135.

42 A. Wang, Z. Chen, Z. Zheng, H. Xu, H. Wang, K. Hu and K. Yan, Remarkably enhanced sulfate radical-based photo-Fenton-like degradation of levofloxacin using the reduced mesoporous MnO@MnO$_x$ microspheres, *Chem. Eng. J.*, 2020, **379**, 122340.

43 Z. Xie, Y. Feng, F. Wang, D. Chen, Q. Zhang, Y. Zeng, W. Lv and G. Liu, Construction of carbon dots modified MoO_3/g-C_3N_4 Z-scheme photocatalyst with enhanced visible light photocatalytic activity for the degradation of tetracycline, *Appl. Catal., B*, 2018, **229**, 96–104.

578 | *Inorg. Chem. Front.*, 2023, **10**, 567–578

This journal is © the Partner Organisations 2023